Nanoscale

Accepted Manuscript

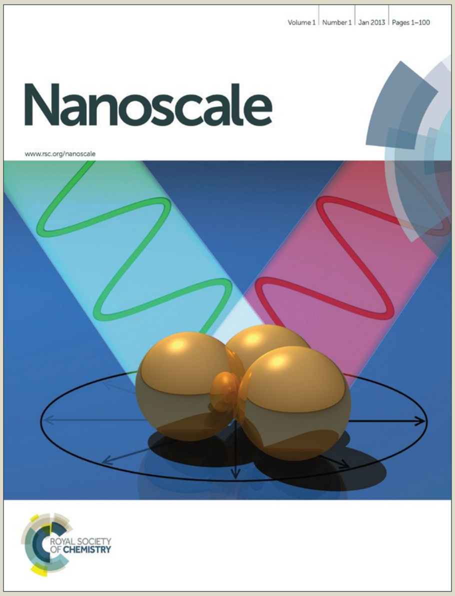

ROYAL SOCIETY OF CHEMISTRY

www.rsc.org/nanoscale

Anomalous liquid imbibition at the nanoscale: the critical role of interfacial deformations

Shaina Kelly, Carlos Torres-Verdín, and Matthew T. Balhoff*
Department of Petroleum and Geosystems Engineering, The University of Texas at Austin,
Austin, TX 78712

ABSTRACT

We observed that imbibition of various wetting liquids in an array of different-sized, horizontal, two-dimensional silica nanochannels terminated within the channels as a function of hydraulic diameter and liquid type. This front termination is not predicted by the classic Washburn equation for capillary flow, which establishes diffusive dynamics in horizontal channels. Various explanations for the anomalous static imbibition measurements were negated; hydrodynamics, thermodynamics, surface chemistry and mechanics were all taken into consideration for this analysis. The atypical imbibition data are explained by deformed menisci and decreased effective channel diameters. These occurrences are due to the nanoscale-enhanced influence of surface forces, thin films, and elastocapillary and solid surface deformation due to meniscus-induced negative pressures (suction) and material stresses. We introduce a phenomenological model which demonstrates how van der Waals forces, common to all interfaces, lead to local menisci deformation and an average reduction in capillary pressure. An expression for the approximate capillary pressure of a symmetric nanoscale meniscus in a cylindrical pore space is derived; its difference from the macroscopic capillary pressure can be expressed by an effective contact angle. Precursor films, adsorbed films and elastocapillary deformation of solid walls decreases effective diameter, exacerbating meniscus deformation and increases in effective viscosity; we also describe local models and effective values for these phenomena. The findings can be scaled to imbibition and two-phase flow in nanoporous media.

Keywords: nanoscale imbibition, nanoscale menisci, elastocapillary deformation, effective viscosity, 2D nanochannels, long-range intermolecular surface forces, effective contact angle, surface stress

INTRODUCTION

Due to the extremely small radii of curvature of nanoscale menisci, capillary pressure is considered to be the dominant force behind flow actuation or imbibition in nanoscale two-phase flow systems.[1] The Young-Laplace equation is a continuum description of capillary pressure commonly invoked in analysis of two-phase flow within porous media and microscale conduits. van der Waals forces, also known as long-range intermolecular forces, and other surface forces (electrical double layer, structural forces, etc.) prevail in thin films of fluid.[2] These thin films are of sub-micron thickness and bounded between other fluids and/or solid materials. van der Waals forces are the sum of the dipole forces between molecules, including London (dispersion interactions), Keesom (orientation or dipole-dipole interactions), and Debye (induction or dipole-induced dipole interactions) forces; thus van der Waals forces account for both electrostatic (polar) and dispersion (nonpolar) effects. The concurrent existence of capillary or bulk surface tension forces and local surface force phenomena in the vicinity of a solid-fluids boundary is accounted for in the augmented Young-Laplace equation.[3] [4] [5] However, in nanoscale conduits surface-force-dominated and transition regions occupy a significant portion of a conduit's volume and can even feel the influence of opposing channel walls,[6] intensifying their effect. Derjaguin performed calculations for polymolecular adsorption and menisci shapes for condensed liquid plugs in narrow pores.[7] "Narrow" is defined as the spacing between parallel plates that results in a complete overlap of long range intermolecular force fields (several nanometers, smaller than the nanochannel widths and heights studied in this work).

Experimental evidence of irregular menisci and breakdown of the Young-Laplace equation have been documented in the literature. Kim et al. observed slower imbibition and multi-curvatures at menisci edges with reduction in channel cross-sectional area for low viscosity polymer flow in 2D nanochannels.[8] Those irregularities in the vicinity of the fluid-solid interface were attributed to long-range intermolecular forces, but rigorous models for this effect were not derived. Honschoten et al. captured an image of a nanoscale water meniscus bridging a surface and an incident probe with an environmental scanning electron microscopy (ESEM); for the given chamber humidity, the radius of the meniscus was much larger than predicted by the macroscopic Kelvin equation (which includes the Laplace pressure assumption in its definition).[9]

While capillary pressure is the dominant flow actuation force at the nanoscale, viscous forces provide substantial resistance to flow. Liquid viscosity is often found to increase from its bulk value at this scale. One explanation for this divergence is the spatial prominence of structured boundary layers, which exhibit increased viscosity on account of surface force-induced ordering. The reported extents of these boundary layers varies greatly in the literature; for example, various experiments with water on hydrophilic surfaces have found a range of boundary layer extents from 0.5 - 150 nm and beyond.[10] [11] [12]

In addition, nanoscale pore or conduit diameters can be highly vulnerable to environmental conditions. The mechanical distortion of confining walls under the influence of stresses provided by capillary forces is known as elastocapillary deformation. This phenomena explains the coalescence of fibrous materials during imbibition[13] as well as the deformation or collapse of parallel plates and nano-and microstructures in the presence of small mensicsi.[14] [15] Elastocapillarity is highly relevant at the nanoscale due to both large capillary pressures and large specific surface areas, the ratio of a pore-space's surface area to volume. Imbibition, capillary condensation, and liquid evaporation all result in menisci and liquid plugs and may lead to a contraction of pores in nanoporous materials.

Consequently, an important nanofluidics question arises: how influential are interfacial interactions and deformations on nanoscale menisci and hydrodynamics, and as a result, fluid imbibition and two-phase flow? Our experimental work on this problem is differentiated from many other nanoscale transport investigations by its use of observable two-dimensional (2D) nanochannels: 2D nanochannels are nanoscale in both cross-sectional height and depth, as opposed to 1D nanochannels or slits which are nanoscale in only one dimension (typically depth).

In a previous publication we developed experimental methods in 2D nanochannels to quantify the effects of nano-confinement on effective values of capillary pressure, liquid viscosity, and gas partitioning across a liquid meniscus.[16] The perfectly wetting liquid isopropanol was used in those experiments. Results indicated that in 2D silica nanochannels there is a significant departure from isopropanol's bulk transport properties and behavior. Specifically, the results included effective capillary pressures at least 40% less than the value predicted by the Young-Laplace equation, a decrease in effective capillary pressure with a decrease in nanochannel size, an on average tenfold increase in effective viscosity from the bulk viscosity, and non-constant interfacial mass transfer coefficients.[16] The increased effective viscosity values were interpreted as highly viscous, virtually nonmoving boundary layer zones extending as thick as 10 - 25 nm from silica surfaces.[16] This is a considerable extent and begged the question of whether concurrent phenomena contribute to the observed increases in effective viscosity. Furthermore, in the absence of an external body force, imbibition fronts characteristically follow the Washburn equation,[17] a power-law trend where the predicted value of the exponent of the imbibition time is 0.5 (a diffusive trend). The isopropanol data revealed that when the imbibing liquids were subject to atmospheric pressure at both the inlet and outlet of the setup, the exponent of the imbibition time trended greater than the predicted value of 0.5 in the nanochannels with the largest cross-sectional areas. These data indicate an unexpected non-constant physical parameter.

The present paper advances phenomenological explanations for the decreased effective capillary pressure values, increased effective viscosity values, and non-diffusive trends. We present imbibition data for various liquids which demonstrate the non-negligible role of fluid and solid interfacial deformations in these miniscule confinements and develop accompanying models that enable descriptions of these deformations.

Background information on the Young-Laplace equation, imbibition, the molecular theory of viscosity, and surface forces are provided in Section 1 of the *Supplementary Information*.

MATERIALS AND METHODS

Figure 1 displays the nanofluidic chip setup. Each chip consisted of two low aspect ratio (one cross-sectional dimension is significantly larger than the other) microchannel/nano-slit pathways and an adjoining array of 2D nanochannels of different sizes. The chips were constructed on a 100 mm diameter silicon wafer with a 1 μm thick layer of silicon dioxide. The fluidic design was written with electron beam lithography on a spin-coated layer of polymethyl methacrylate (PMMA). Reactive ion etch (RIE) was used to transfer these pattern into the silica. Subsequently, thru holes were created and the oxidized silicon wafer was anodically bonded to a 200 μm thick borosilicate glass wafer after both substrates are cleaned with a piranha solution. Piranha solution (4:1 H_2SO_4/H_2O_2) is a strong oxidizing agent that is especially useful for removing organic contaminants from surfaces. In addition, oxidizing agents add hydroxyl groups to a substrate's surface (silanol groups in the case of glasses/silica). Clean and hydroxylated surfaces correspond to hydrophilic or lyophilic wetting conditions. Finally, the bonded wafers were diced into a batch of approximately 20 mm-wide square nanofluidic chips.

The nanochannels are all 60 nm in depth and range in width from 30-500 nm. Specifically, the widths of the 20 nanochannels are (triplicates and duplicates of certain channel widths are indicated in parenthesis): 30, 40, 50 (3), 60, 70, 80, 90, 100 (2), 120, 150 (3), 175, 200 (2), 250, and 500 nm. The nanochannels exhibit surface roughness characteristic of RIE and 85° sidewall tapering, which renders them slightly trapezoidal in cross section; both of these artifacts are typical to dry etching processes such as RIE. Mannion et al. reported nanochannel floor roughness (hillocks) of 10-20 nm as a result of RIE.[18] Figure

1.C depicts an idealized cross section of one of the nanochannels. The channels are 250 μm long, *L*, which, combined with a nanoscale cross-section, results in extremely high hydraulic resistivity. Still, the liquid capillary pressure in these channels is theoretically, per the Young-Laplace equation, strong enough to traverse the entire 250 μm length in less than a second, even with substantial and increasing viscous drag. Experimentation with a variety of liquids enables a comparison of imbibition anomalies on the basis of fluid properties.

Optical fluorescent microscopy was used to observe the movement of liquid-gas interfaces of various liquids within the predominantly silica nanofluidic chips. Only the location of fluid interfaces in 2D nanochannels can be captured with optical microscopy; the widths of these nanochannels are near the resolution of an optical microscope (this resolution is limited by the wavelength of light and numerical aperture of an objective), and menisci curvatures cannot be discerned from images. The liquids observed were deionized (DI) water, brine (0.05 M NaCl mixed in a 50%:50% ratio with methanol), isopropanol, acetone, methanol, heptane, and decane while the non-wetting fluid was air. All liquids were doped with Rhodamine B (Sigma-Aldridge), $C_{28}H_{31}ClN_2O_3$, a neutral fluorescent tracer molecule, and captured with a Zeiss Axiovert 200M fluorescent light microscope (FLM).

Powdered Rhodamine B was dissolved into the designated solvents to a solute concentration of 100 μM and magnetically stirred. Note that Rhodamine B is most soluble in alcohols and water and exhibits low solubility in hydrocarbons. Rhodamine B is excited by ultraviolet light (UV) and a visible light wavelength peak of 540 nm and emits light (fluoresces) at a maximum wavelength peak of 625 nm with a full width at half maximum (FWHM) of approximately 10 nm. These peaks can shift slightly depending on the solvent the fluorophore is dissolved in. A UV-Longpass filter cube was used in the Zeiss Axiovert 200M to satisfy the excitation and emission criteria, given that the Longpass has a narrow 12 nm band of excitation light, which peaks at 365 nm (UV range) and is sensitive to all emission wavelengths above 397 nm. A TRITC filter cube, which has an excitation bandpass of around 530 - 550 nm and an emission bandpass capture of around 570 - 615 nm, was also used in the experiments.

As displayed in Figure 1.A, the nanofluidic chips have four inlet/outlet holes. Liquids are introduced to the nanofluidic chips by administering 2 μL droplets to one of the inlet holes with a micropipette. Nanofluidic chips were open to the atmosphere and at room temperature. Tested liquids naturally imbibed into the 1000 nm high nano-slits with the exception of water which required a syringe pump and tubing connection system for fluid entry. The experimental difficulty with water, the tested liquid with the greatest surface tension, was *entering* the narrow chip inlets. The issue may have been exacerbated by the inevitable accumulation of particulates at the inlet apertures. Water did spontaneously imbibe (though anomalously, as described in this work), once introduced into the nanofluidic chips.

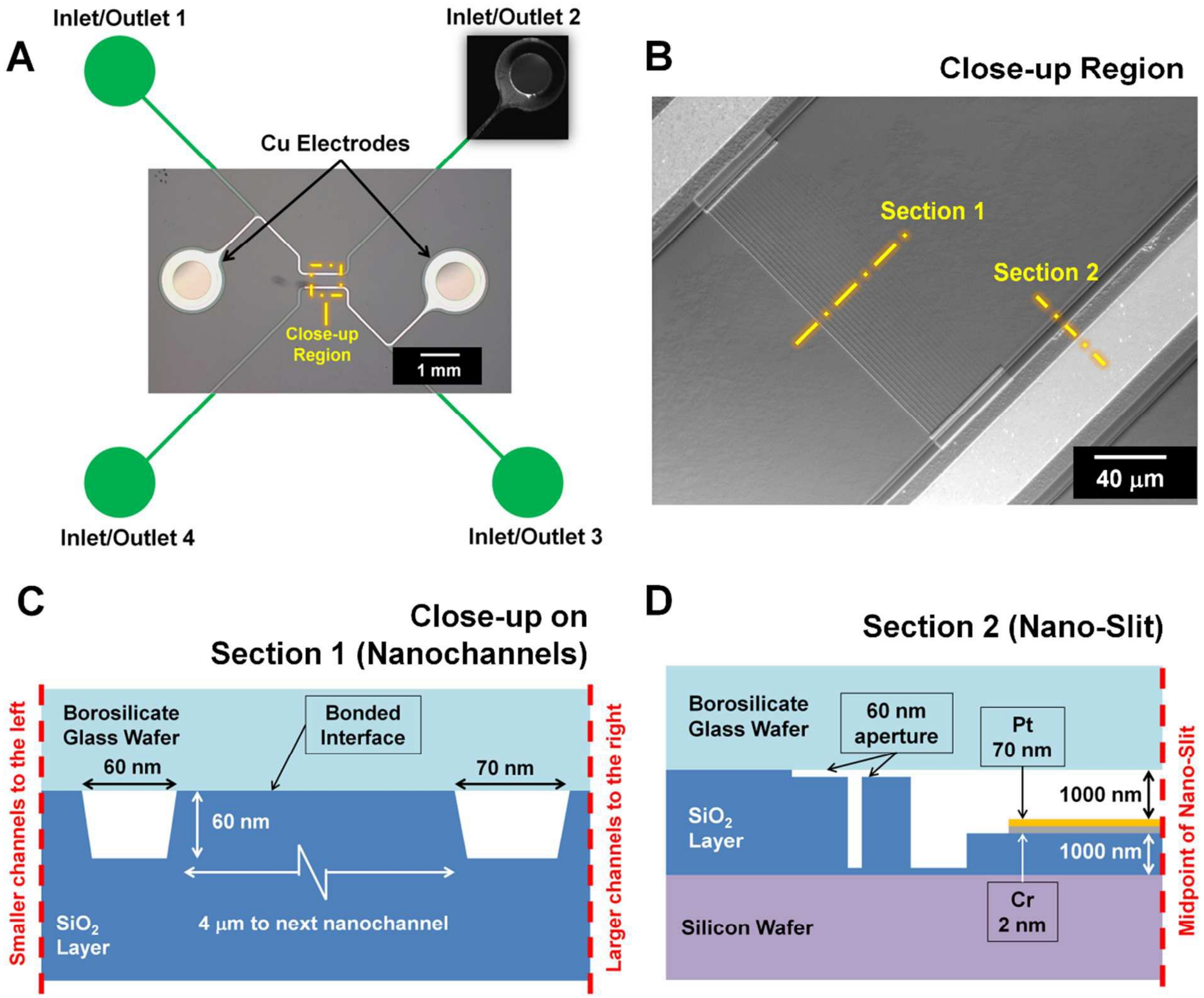

Figure 1. (A) Schematic of the nanofluidic chip design with an inset brightfield microscopy image of the fluidic network of two low aspect ratio microchannels/nano-slits with an array of nanochannels connecting them. The copper electrodes flanking the nano-slits were not utilized in this work. (B) Reflected differential interference contrast microscopy images of a nanochannel array and adjoining low aspect ratio microchannels (nano-slits) in one of the nanofluidic chips. (C) Schematic cross sections (not to scale) of two of the nanochannels. (D) Schematic cross sections (not to scale) of half of a nano-slit. Thin layers of chromium (Cr) and then platinum (Pt) were sputtered onto portions of the low aspect ratio nano-slits. The original purpose of the metal films and the unusual configuration of the nano-slits were for the creation of the aforementioned electrical connections; again, measurements with these electrodes were not explored in this work.

The Zeiss Axiovert 200M is a widefield inverted fluorescent microscope, uses a 100 W mercury lamp as its light source, and captures images with a Zeiss CCD camera interfaced with a desktop computer. 20X (air) and 100X (oil immersion) objectives were used for large field of view and close-up perspectives, respectively. A restrictive frame rate of approximately one frame per second (fps) rendered the capture of consistent velocity data in the nanochannels challenging; thus, for consistency, imbibition in the nanochannels is discussed in terms of the imbibed lengths at which fluids reached an equilibrium point.

Image analysis of the locations of liquids in the nanofluidic chips was performed using ImageJ/Fiji (National Institutes of Health). The location of the fluorescing fluid was distinct against the opaque background of the silicon wafer material (see Figures 2 and 5 for examples). Fluid was assumed to be wherever fluorescence was detected, even if the fluorescent intensity waned at the tip of the front (for example, see Figure 2.D); such regions may correspond to precursor films.

To help prevent chip fouling, the nanofluidic chips were subject to solvent (isopropanol and acetone) "flushes" with a syringe pump between uses, sonication, and soaking in the aforementioned solvents for prolonged periods of time (diffusion-based cleaning). Despite these efforts, it was found that once a nanochip is exposed to Rhodamine B, complete removal of the fluorophore is problematic. Such residual Rhodamine B may lead to additional surface roughness and, as a result, lower hydraulic conductivity in the nanofluidic system and channels. Most experiments from the presented data were performed on brand new chips and these results are designated with an asterisk in Figure 3.

RESULTS

Imbibing liquids were observed to significantly slowdown and cease movement within the nanochannels; an example of this stymied movement and front cessation is displayed for heptane in Figure S1 of the *Supplementary Information*. Dynamic imbibition is not studied for all of the liquids in this work and the results are presented in terms of anomalous front termination lengths, l_t. Termination lengths generally increased with nanochannel width, and in most of the array's smaller channels l_t was far shorter than 250 μm. Figure 2 shows visual examples of such termination lengths, while Figure 3 compares the termination lengths of the different fluids studied along the range of nanochannel hydraulic diameters, D_H, where $D_H = 4 \times A/P$ (A is cross sectional area and P is perimeter). Results for the 0.05 M NaCl/methanol mixture are displayed and reveal that the mixture imbibes less than DI water; however, this liquid is not further analyzed due to its compositional complexity.

Figure 2.C and D appear to illustrate channel roughness/unevenness as opposed to "smoother" fluorescing profiles in Figure 2.A and B. Brighter areas represent either (1) areas of greater fluorophore concentration, or (2) areas of less exposed (photobleached) fluorophores. Hence, the lighter front extents in Figure 2.D most likely represent prewetting films or collapsed regions with less liquid volume (and fluorophores) present. The channels are not atomically smooth, but the unevenness perceived with fluorescent imaging in some of the images (i.e. the bottom of Figure 2.D) is a non-physical microscopy artifact. Fluorescent microscope settings and fluorophore solubility ranged among experiments and fluids and, thus, should not necessarily be used as a basis of comparison.

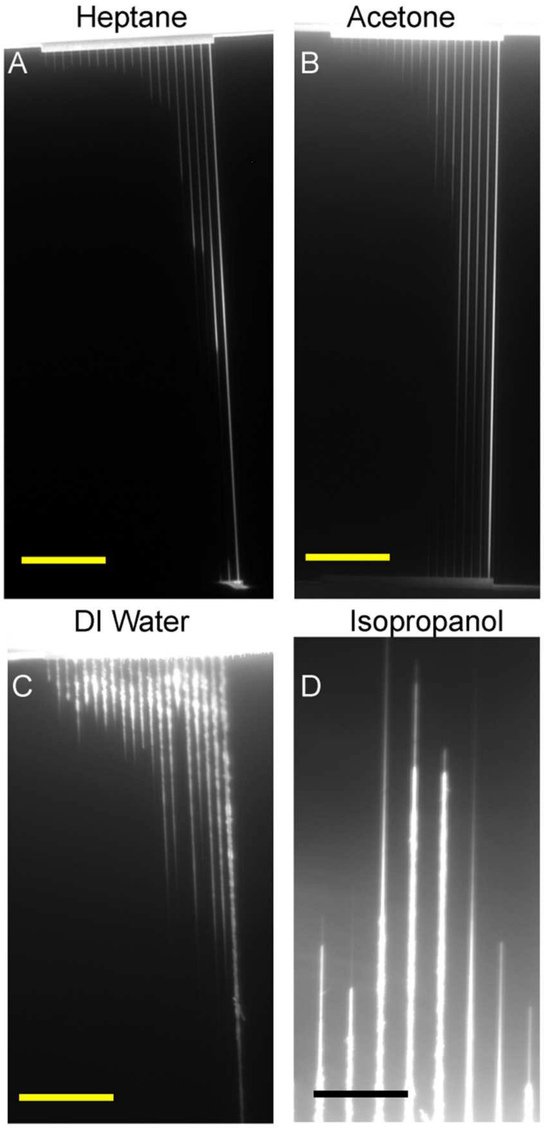

Figure 2. All fluids were doped with Rhodamine B and images are captured with a Zeiss Axiovert 200M FLM. The fluorescent signal makes the nanochannels appear larger than their actual size. (A) - (C) Imbibition termination lengths of labeled experimental fluids captured with a 20X objective. The scale bar is 40 μm for these images. Nanochannel sizes increase from left to right from 30 × 60 nm to 500 × 60 nm in cross section. (D) Imbibition termination lengths of isopropanol within nanochannels in the middle of the array captured with a 100X objective; scale bar is 12 μm. This close-up image exhibits a change in fluorescent intensity at the tips of the imbibition fronts, an observation often seen in the experiments that may correspond to a pre-wetting film. Alternatively, channel buckling and opposite wall contact may be the cause of such areas of decreased fluorescent intensity. The imbibition front in the largest nanochannels frequently made it to the opposing nano-slit reservoir, and, as a result, some imbibition did occur from the opposing reservoir back into the nanochannels. However, the volume-limited effect of imbibition from the opposing reservoir is not a prime issue because these opposing fronts occurred after the primary imbibition fronts in the smaller nanochannels had significantly slowed down or reached their termination lengths. In addition, the return of imbibed fluid from the opposing reservoir is clearly not the prime cause of the non-diffusive imbibition termination fronts because such termination occurred ubiquitously in the experiments, including in channels without such return of imbibed fluid.

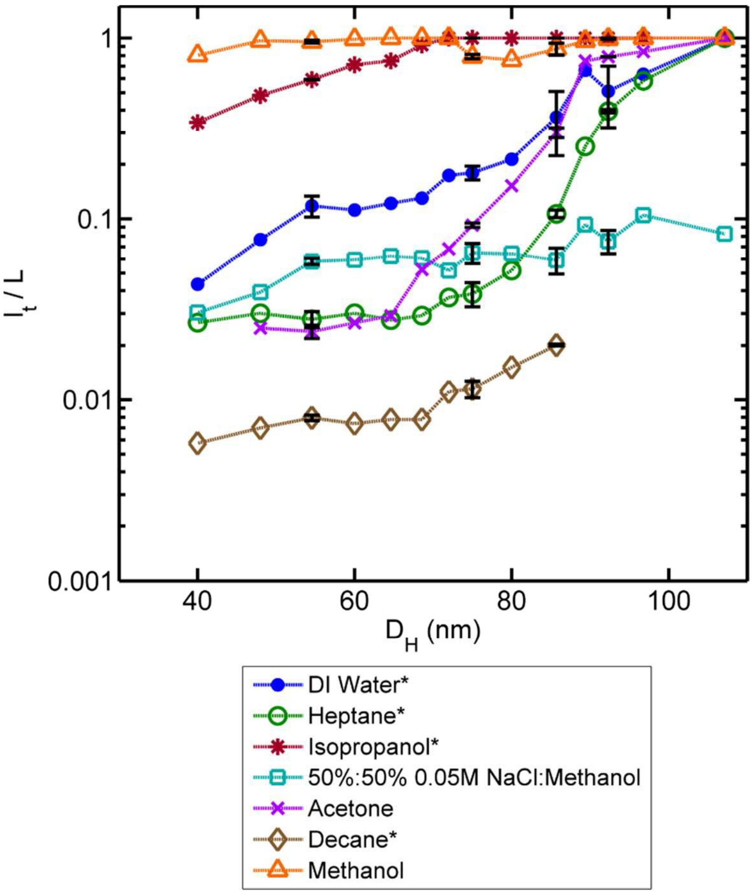

Figure 3. Ratio of imbibition termination length (l_t), as detected by Rhodamine B fluorescence, over total length of the nanochannel array (L = 250 μm) versus hydraulic diameter of the nanochannels for the tested fluids. Liquid droplets were administered to a chip inlet (see Figure 1) and freely imbibed into the nanofluidic chips from that inlet while all other inlets/outlets were left open to the atmosphere. Termination length varied considerably from smallest to largest channel and between different imbibing liquids. Aqueous salt solutions did not readily imbibe into the nanofluidic chip; methanol was added to increase wetting. No data were obtained for decane in the larger nanochannels. Asterisks designate experiments performed on new chips. Error bars are derived from results in duplicates and triplicates of particular channel sizes and display some dispersion for the relatively larger channels.

The relative transport success of the liquids as a whole into the nanochannel arrays is summarized as a saturation fraction, S_w, for comparison against bulk liquid properties. S_w is the ratio of the total volume of wetting fluid imbibed into the array of 20 nanochannels to the total volume of the nanochannel array; e.g.

$$S_w = \frac{\sum_{i=1}^{20} w_i \left(l_t\right)_i}{L\sum_{i=1}^{20} w_i}\ , \ (1)$$

where w is the nanochannel cross sectional width; h, nanochannel depth, cancels out because it is the same for all of the channels. Table 1 displays values of S_w and relevant bulk liquid properties for comparison. We find that S_w is not correlated to published bulk values of liquid viscosities, macroscopic silica-liquid contact angles, molecule weight/size, etc. Furthermore, S_w and the imbibition extents are not clearly correlated to combinations of these bulk physical values, such as the dimensionless capillary number (Ca), $\mu V/\gamma$ (where V is the velocity of the fluid). There is also no correlation between the estimated pressures in the liquids due to viscous losses at the termination lengths and saturated vapor pressures of the liquids at room temperature (at these pressures liquids evaporate). With the exception of DI water, the compared values of surface tension do not significantly vary among the other fluids; a trend between wetting fluid saturation success and decreased surface tension is not present (see S_w and γ values in Table 1).

Examination of the properties of the different imbibing liquids at an intermolecular forces level suggests a robust correlation between nanochannel imbibition success and the Hamaker constants of the system, A_{232} and A_{123}. These constants are representative of the strength of van der Waals interaction forces for, respectively, two films of the same liquid acting across a film of air and a solid and air acting across a film of said liquid. Hamaker constants, generally referred to as A_H, allow molecular interactions to be considered from a continuum perspective and are dependent on fluid and material properties; more details on A_H are included in Section 3 of the *Supplementary Information*. Figure 4 displays a cross-plot of the values of A_{232} and S_w for the liquid-air-liquid systems in the nanochannels. The outlier to the trend is isopropanol. The value for isopropanol is most likely an outlier based on its (a) polarity and (b) precursor film thickness. The pore space available for a fluid meniscus and mass flux becomes smaller in the presence of, respectively, relatively thick precursor films and adsorbed layers. Isopropanol has lesser extents of these films and layers compared to methanol, which has a lower A_{232} value, but a very similar S_w results. In more detail,

(a) The surface charge of oxides such as alumina and silica increases in polar liquids.[19] To achieve electroneutrality, a larger amount of molecules may accumulate in boundary layers for surfaces of greater negative interfacial potential or charge density. Isopropanol, followed by methanol, is the least polar of the tested polar fluids and theoretically forms a thinner layer of absorbed molecules than methanol.

(b) The greater the negative value of A_{123}, which corresponds to the van der Waals forces between a solid and gas across a liquid film, the greater the propensity of a precursor film or meniscus edge to thicken. The value of A_{123} for isopropanol is notably smaller than that of methanol and thus, isopropanol may have smaller precursor films.

Refer to Figure S2 of the *Supplementary Information* for examples of experimental dispersion in fouled (used) chips. Further experimental observations of interest in the nanochannels as well as observations of film-like flow in the nano-slits are included in Sections 7 and 8 of the *Supplementary Information*.

Table 1. Properties of the experimental fluids and average saturation data.

Fluid	S_w†	γ (mN/m)	θ_0* (°)	μ (10^{-3} Pa s)	ρ (kg/m^3)	*Mw* (g/mol)	P_v (kPa)	μ_D (D)	n	ν_e (10^{15} Hz)	ε	A_{123}** (10^{-20} J)	A_{232}** (10^{-20} J)
Isopropanol	**0.95**	23.8	0	1.96	786.00	60.10	6.02	1.56	1.38	3.1	18.2	-1.04	4.20
Methanol	**0.94**	22.6	0	0.590	791.80	32.04	16.9	1.69	1.33	3	33.1	-1.22	3.68
Acetone	**0.51**	23.7	6	0.308	791.00	58.08	30.6	2.91	1.36	2.9	21	-1.08	4.08
DI Water	**0.48**	72.8	28	1.00	999.97	18.02	3.15	1.85	1.33	3	80	-0.98	4.35
Heptane	**0.15**	20.1	0	0.386	684.00	100.21	6.13	0	1.39	3	1.89	-0.91	4.53
Decane	**0.01**	23.8	0	0.920	730.00	142.29	0.17	0	1.41	3	2	-0.70	5.04

Symbol Key: S_w = saturation of the wetting fluid; γ = surface tension; θ_0 = macroscopic contact angle; μ = viscosity; ρ = density; *Mw* = molecular weight; P_v = vapor pressure; μ_D = dipole moment (unit = debye); n = index of refraction; ν_e = absorption frequency; ε = dielectric constant; A_{123} = Hamaker constant for the fluid between silica and air; A_{232} = Hamaker constant for air between two layers of the fluid

† [Total volume of wetting fluid imbibed into the nanochannel array] / [total volume of the nanochannel array]

* Macroscopic contact angle on polished quartz (silica) from Ethington (1990).[20] The contact angles of heptane and decane on quartz were not found in the literature, but were assumed to be zero like the other spreading/wetting fluids. All of the fluids are wetting.

** The Hamaker constant is calculated using the macroscopic Lifshitz calculation. The literature contains experimentally derived values, which can slightly differ from these predictions.

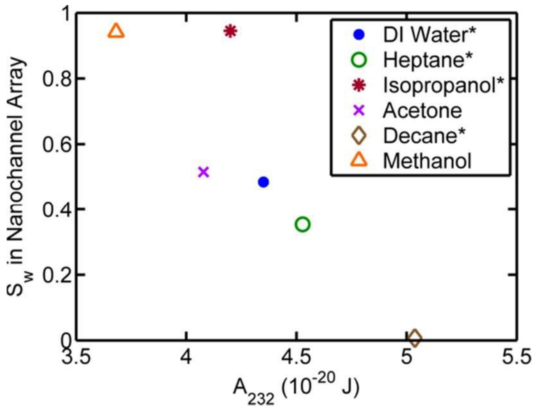

Figure 4. The data suggest a trend between imbibition success, summarized by S_w, and calculated Hamaker constants for a system of two films of liquid (fluid 2) interacting across a film of air (fluid 3), A_{232}. The value of A_{232} is always positive, which indicates an attractive force between the like liquid films and a propensity for the enclosed air film to thin. Such attraction may lead to deformation of a nano-confined meniscus. Note that the data also trend with the absolute value of A_{123}, indicating that precursor film thickness may play a prominent role in nanoscale imbibition. The value for isopropanol is an outlier from both perceived trends (see explanation in the *Results* section). Experimental and calculated values of the Hamaker constant can slightly differ.

DISCUSSION

Theories for the varying termination lengths in the nanochannels and the atypical progression of menisci in the nano-slits draw from hydrodynamic, thermodynamic, mechanical, and surface chemistry principles. We reviewed the compatibility of these theories with the data and discuss and negate many of them subsequently. Overall, the inability of many of the liquids to completely traverse the majority of the nanochannels are best explained by two concurrent phenomena:

(a) The influence of surface forces, specifically van der Waals forces, on a nanoscale meniscus can lead to deformation of the meniscus and an effective P_c value lower than the macroscopic Young-Laplace value.

(b) Deformation of the channel walls by elastocapillary effects result in smaller effective channel (or pore) diameters. This shrinkage corresponds to decreases in hydraulic conductivity, potential increases in effective viscosity, and intensification of effect (a).

Phenomenological models for (a) and (b) are presented later in this section.

Leakage, fluorophores, and dynamic contact angles

A lack of Rhodamine B fluorescence between parallel nanochannels signifies that leakage of fluid along the silica-borosilicate glass bonding interface is unlikely in the imbibition data examined. However, liquid leakage cannot be detected in possible apertures at the bonding interface that are smaller than 1.7 nm in height, the length of a Rhodamine B molecule [21]. Yet, leakage is improbable because decane, which has a molecular length of approximately 10 Å,[22] imbibed the least. Decane molecules can barely fit more than one at a time into an aperture less than 1.7 nm; hence, decane, though displaying minimal imbibition, is the least likely to be prone to leakage in sub-nanometer apertures. Large dynamic contact angles were first suspected to be the cause of stymied imbibition in the nanochannels.[23] Dynamic contact angles are greater than static contact angles, and their departure from a static contact angle value positively scales with *Ca* or imbibition velocity.[24] However, the termination lengths in the nanochannels do not correlate with *Ca*; it was observed that liquids that imbibed the fastest also imbibed the farthest, indicating that dynamic wetting failure does not explain the results presented herein. It was initially a major concern that the neutral tracer Rhodamine B may have effects on hydrodynamic transport and menisci. However, we achieved similar stymied isopropanol imbibition results to that with FLM using the same nanofluidic chip design and differential interference contrast microscopy (DIC), a tracer-free method. We detailed these results in a previous nanofluidics publication.[16] In addition, on several occasions tracer-free fluid was imbibed into the chips and Rhodamine B subsequently injected; the fluorophore diffused to a length within the experimental error of the termination lengths (see error bars in Figure 3) observed during imbibition with the fluorophore. Because Rhodamine B is a neutral molecule, it is expected that its effect on surface tension will be less than that of a charged molecule or surfactant, which lower surface tension.

Precursor films

Wetting fluids lead to greater imbibition extents, but result in longer and thicker wetting fingers,[25] which can decrease effective nanochannel diameter. These precursor films are aspect ratio dependent and are found to form more prominently in narrow rectangular channels,[25] [26] such as 1D nanochannels. The fingers rise faster and farther than the meniscus and follow a different power law trend ($l \sim t^{1/3}$).[27] In vertical micro-tubes the presence of long precursor films in front of menisci decreases the vertical equilibrium height of a meniscus to approximately 0.94 of its predicted value.[28] A potential cause of stymied imbibition in nanochannels is the formation of enclosed bubbles when pre-wetting films or "capillary fingers" proceed ahead of the meniscus and thicken.[29] However, the likelihood for pre-wetting film thickening, described by the Hamaker constant for the system of a liquid between silica and air, A_{123}, trends with imbibition success, S_w. Thus, it is surmised that the effect of precursor film thickening may encourage nanoscale imbibition by preventing film rupture in the presence of surface roughness and other inhomogeneities. Figure 2.D (isopropanol, A_{123} = -1.04 × 10^{-20} J) and Figure 5.B (heptane, A_{123} = -0.91 × 10^{-20} J) show evidence of respectively, intact and ruptured prewetting films.

Metastability and cavitation

The inlets and outlets of the nanofluidic chips were open to the atmosphere, which means that the gas/air pressure at the endpoints of the imbibing liquid, P_0, was atmospheric, 101.325 kPa. Pressure in the imbibed liquid drops linearly and the pressure gradient changes with the length imbibed, given by

$$\frac{\Delta P}{l(t)} = \frac{P_0 - P_c}{l(t)} \; . \quad (2)$$

The theoretical liquid pressure in the 2D nanochannels behind the meniscus per the Young-Laplace equation is approximately -0.7 to -2 MPa (from largest to smallest nanochannel) for all of the liquids. Thus, liquid pressures throughout the nanochannels will likely fall below their saturated vapor pressures and below zero (see Figure 6.B). Liquids existing at pressures below the saturated vapor pressure line and negatively pressured liquids are in the metastable region of a substance's thermodynamic phase diagram. These liquids are theoretically in tension, meaning the liquid molecules exist in a fragile, stretched state [30] [31] [32] and pull on the walls of their confinement.[33] In this state, liquid menisci may also be more subject to deformation by boundary layer effects (long range intermolecular forces) as well as dewetting and pinning. At certain high negative pressures the tensile strength of a molecule is reached and a liquid transitions to vapor; this point is called the spinodal pressure. Negatively pressured liquids in the nanochannels described herein are nowhere near their spinodal pressures (for example, the spinodal pressure of water at room temperature is between -150 and -250 MPa),[34] and hence phase transitions due to tensile strength limits (boiling) are not a possibility in the experiments.

A liquid typically experiences cavitation, the formation of vapor bubbles within the liquid, when its pressure, P_l, drops below its saturated vapor pressure, P_{sat}, for a particular temperature. Impurities, seeding, or preexisting bubbles can trigger cavitation. In nano-confinements this cavitation is not always possible due to the instability of very small bubbles below a critical radius, r_c, (that is, these bubbles collapse), given by[35]

$$r_c = \frac{2\gamma}{P_{sat} - P_l} \; . \quad (3)$$

Nano-confinements whose smallest critical dimension is below r_c have the ability to maintain large negative pressures on the liquid side of a meniscus because bubbles are not energetically sustainable (see inset cartoon in Figure 5). The theoretical *maximum* liquid pressures in the nanochannels due to predicted menisci curvatures correspond to critical bubble diameters of approximately 40 nm in the 30 × 60 nm channel and 120 nm in the 500 × 60 nm channel (Eq. 3 is fairly insensitive to fluid type when $P_l >> P_{sat}$ and γ values are similar). The proximity of the critical bubble diameters to the cross sectional dimensions of the smallest nanochannels in the array indicates that nucleation of bubbles is possible in the realm of a meniscus within these channels, but not certain. While cavitation can stymie the imbibing front, it does not explain the evident difference in termination lengths among the different liquids and in the relatively larger nanochannels.

The fluorescent microscopy image data indicate that the presence of large bubbles/gas slugs can be detected within the nanochannels. Figure 5.B displays what a front looks like when there are both liquid and gas states present in a front film – either by way of evaporation, precursor film rupture, or even cavitation. This image was taken of heptane in a 500 nm × 60 nm channel with a 100X objective from an experiment in a previously used chip where one of the reservoirs was blocked. None of the data included in this analysis had such a ruptured/evaporative front. Figure 5.A shows an image of the front of imbibed methanol in a 500 nm × 60 nm channel also taken with a 100X objective. In this case, a diffuse ruptured film is not present, but there is evidence of a lone bubble (potentially cavitation). Thus, the optical microscopy data suggests that cavitation is possible, especially in the larger nanochannels of non-uniform cross sections, but that it is not widely observed. Indeed, Zhang et al. found from simulations that cavitation is more likely in non-uniform nanochannel cross sections.[36] Figure S9 of the *Supplementary Information* also shows examples of how gas slugs appear in the images of the nanochannels. The cavitation observed in 1D nanochannels in the work of Duan et al. resulted in long gas slugs;[37] such slugs would be obvious in the nanochannels examined in this work.

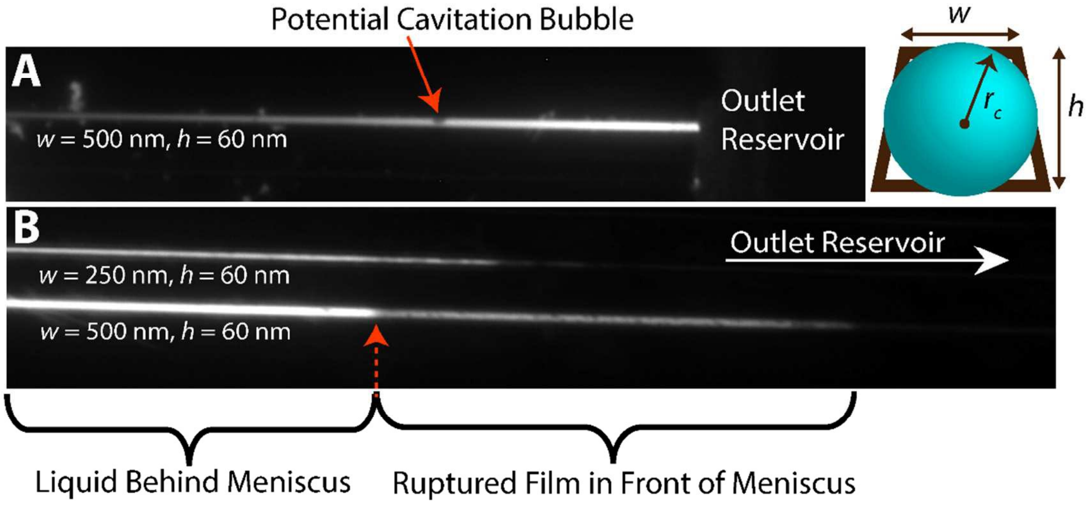

Figure 5. (A) Methanol in a 500 nm × 60 nm channel displays a potential cavitation bubble. Methanol readily reaches the channel outlet, but does not enter the outlet reservoir. Fluorophores appear to accumulate at the stopped front. *Inset*: illustration of the case where the critical radius of an energetically stable bubbles (r_c) is larger than a nanochannel's shortest dimensions and, thus, is not expected to form. (B) Heptane in a 500 nm × 60 nm channel displays with a closed outlet reservoir displays an evaporating or ruptured precursor film. The spacing between parallel nanochannels is 4 μm.

Boundary layer viscosity

We also considered the effective increase in liquid viscosity due to attraction of molecules to the walls of the nanochannels through long-range intermolecular forces. A simple model was employed: Eyring's liquid viscosity theory [38] was modified to account for an addition to the free energy of activation, ΔG_I, for a liquid molecule in the presence of an interface, given by

$$\mu_{nano} = \left(\frac{\delta}{a}\right)^2 \frac{\tilde{N}\hbar}{\tilde{V}} \exp\left(\left(\Delta G_0 + \Delta G_I\right)/k_B T\right), \quad (4)$$

where k_B is Boltzmann's constant, δ is the distance between molecular layers, a is length of jump a molecule must make to get to a vacant space, $\tilde{N}$ is Avogadro's number, $\hbar$ is the Planck constant, $\tilde{V}$ is liquid molar volume, R is the gas constant, T is temperature, and ΔG_0 is the free energy of activation for a molecule to escape from a "cage" of neighbor molecules. The ratio of Eq. 4 and the unmodified version of Eyring's equation results in a cancelation of like terms and the expression

$$\frac{\mu_{nano}}{\mu_{bulk}} = \exp\left(\Delta G_I / k_B T\right). \quad (5)$$

ΔG_I is described in terms of the force between a macroscopic body (solid wall) and a molecule, i.e.,[39]

$$\Delta G_I = \frac{\pi \rho_s C_{ls}}{6D^3}, \quad (6)$$

where D is distance between the molecule and the solid interface, ρ_s is molecular number density of the solid, and C_{ls} is the van der Waals interaction constant in units of J-m^6 between liquid and solid molecules (a system's Hamaker constant is equal to $\pi^2\rho_l\rho_s C_{ls}$, where ρ_l is molecular number density of the liquid). Thus, viscosity is a function of distance from a channel wall. However, because Eq. 5 is an exponentially decaying function, this model only results in notable viscosity increases out to a distance of one or two nanometers from a surface. Consequently, μ_{nano} can theoretically be over an order of magnitude larger than μ_{bulk} in nanopores with diameters around several nanometers and less, but the effect of long-range intermolecular forces on viscosity is not large enough in the investigated nanochannel sizes to account for the observed l_t values. Lui and Li (2011) performed molecular dynamics simulations on the topic of nanoscale viscosity and confirm that flow rate, which is dependent on viscosity, can show notable variance from the macroscopic value in channels of $D < 30$ nm with increases in fluid-wall binding energy (analogous to ΔG_I) and particularly diverges when $D < 5$ nm.[40]

Model for a nanoscale meniscus

We construct a composite film model of a nanoscale meniscus (see Figure 6.A) to theoretically investigate the effect of long-range intermolecular surface forces on menisci in 2D nanochannels. Each film or channel material is numerically labeled: material 1 is the silica channel surface, material 5 is either silica or borosilicate glass (respectively, the side walls or the top of the channels), films 2 and 4 are opposing edges and/or precursor films of the liquid meniscus, and film 3 is the air confined within the meniscus curvature and between precursor films. In larger confinements, such as microchannels, the non-wetting fluid would not be considered an interior thin film. Hamaker constants mixing rules for any film (labeled b) combined between two other films or solids (labeled a and c) are as follows:[41]

$$A_{abc} = \left(\sqrt{A_{aa}} - \sqrt{A_{bb}}\right)\left(\sqrt{A_{cc}} - \sqrt{A_{bb}}\right), \quad (7)$$

and

$$A_{abc} \approx \pm\sqrt{A_{aba}A_{cbc}}\ . \quad (8)$$

The adhesion ($A_{abc} > 0$) or repulsion force ($A_{abc} < 0$) per unit area due to van der Waals interactions, Π, across a single medium confined between infinite parallel plates separated by a distance d is the derivative of the free energy per unit area, G:[42]

$$\Pi(d) = \frac{F(d)}{Area} = -\frac{\partial G}{\partial d} = \frac{-A_H}{6\pi d^3}\ . \quad (9)$$

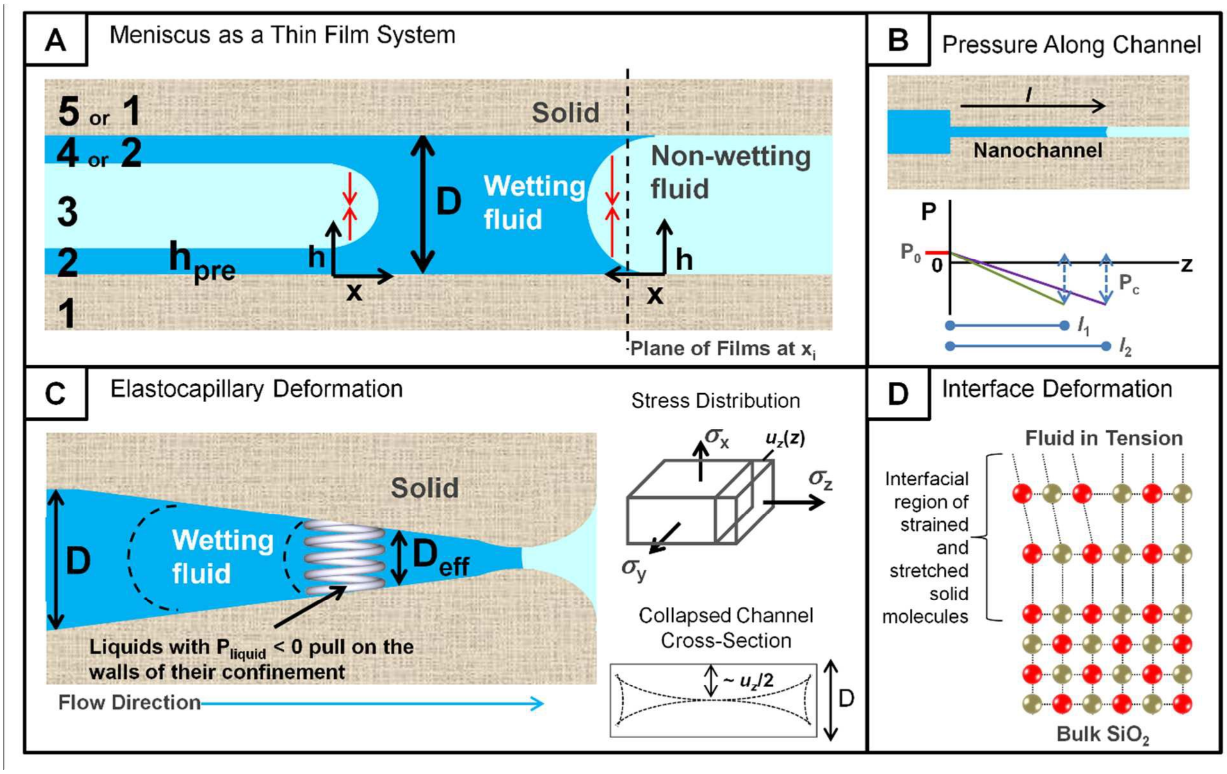

Figure 6. (A) Diagram of two possible configurations of a nanoscale meniscus where the meniscus is considered as a system of composite films/materials in a 2D nanopore or nanochannel space of diameter, D. A wetting film of height h_{pre} (shown with the left meniscus) may be present. The thickness of films 2, 3, and 4 vary as a function of x along the meniscus. Height, h, and curvature of the meniscus may vary from the semicircular curves illustrated due to the influence of surface forces (net force is depicted with a red arrow). (B) Pressure drops along a nanochannel are mathematically negative when $P_c >> P_0$. (C) Metastable and negatively pressured liquids generate a suction effect within a pore space; dotted lines represent changing menisci profiles. (D) Additional deformations occur at the interfacial zone of a solid (cartoon adapted from Weissmüller and Kramer [2010])[43].

The net van der Waals interaction force per unit area *between* two surfaces for the proposed composite (multilayer) film system, Π_s, is calculated as follows:[44 45]

$$\Pi_s(d,h_1,h_2)=\frac{-A_{234}}{6\pi d^3}+\frac{\sqrt{A_{121}A_{343}}}{6\pi\left(d+h_1\right)^3}+\frac{\sqrt{A_{545}A_{323}}}{6\pi\left(d+h_2\right)^3}-\frac{\sqrt{A_{121}A_{545}}}{6\pi\left(D\right)^3},\quad (10)$$

where D is the total width of an examined cross section, d is the thickness of the enclosed gas (film 3), and h_1 and h_2 are the thickness of films 2 and 4, respectively. Note that, even in the absence of a meniscus, Π_s can lead to pore wall deformation for very small (near-Angstrom) nanopore spaces when it is on par with the strength of the pore material. The net van der Waals interaction force per unit area acting on film 2 for the proposed composite (multilayer) film system, Π_m, is calculated as follows:[7, 45]

$$\Pi_m(d,h_1,h_2)=\frac{-A_{123}}{6\pi h_1^3}+\frac{A_{234}}{6\pi d^3}-\frac{\sqrt{A_{545}A_{323}}}{6\pi\left(d+h_2\right)^3}.\quad (11)$$

Up to its midpoint, a 2D meniscus is regarded as a film of varying thickness, and, for mathematical simplicity, the 2D profile is considered to depend on one coordinate, x, such that,[5]

$$P_c=\gamma\kappa\approx-\gamma\frac{d^2h}{dx^2},\quad (12)$$

where $h(x)$ describes the meniscus profile along a cross section up to the meniscus midpoint and x runs along the solid channel surface. The axis origin is aligned with the point where the meniscus curvature begins. We assume that the meniscus shape does not change during imbibition (a quasi-static or “rigid” meniscus; no dynamic effects). We then consider the film system to be symmetric (material 1 is the same as material 5 and film 2 is the same as film 4) such that $h_1 = h_2 = h$ and $d = D - 2h$ and, given the mixing rules of Eq.’s 7 and 8,

$$\Pi_m(h,D)=\frac{1}{6\pi}\left(\frac{-A_{123}}{h^3}+\frac{2A_{232}}{\left(D-2h\right)^3}-\frac{A_{123}}{\left(D-h\right)^3}\right).\ (13)$$

An equilibrium equation is necessary to solve for the local meniscus curvature due to the presence of surface forces as a function of D and h. In the case of a nanoscale meniscus that is only partially deformed and retains some portions of constant (bulk) curvature, the applicable expression is:

$$P_c^m=\gamma\kappa_n+\Pi_m(D,h),\quad (14)$$

and

$$P_c^n=\gamma\kappa_n,\quad (15)$$

where P_c^m is the macroscopic capillary pressure predicted by Young-Laplace’s equation for a planar aperture and the local meniscus curvature, κ_n, and Π_m change along the meniscus with changes in the lengths of h and d; P_c^n is the local nanoscale capillary pressure. From Derjaguin’s work on menisci in narrow slits, a symmetric meniscus is in equilibrium with a precursor film of height h_{pre} such that,[7]

$$\Pi_f(h_{pre})=\gamma\kappa_n+\Pi_m(D,h),\quad (16)$$

where Π_f is the force per unit area due to van der Waals interactions across the precursor film; Π_f can be set to the same value as P_c^m for a first-hand estimation or can be determined with disjoining pressure isotherms or the Langmuir equation for absorption.[45] The pore space available for a fluid meniscus becomes smaller in the presence of relatively thick adsorbed or precursor films. Overlapping surface force layers can lead to additional widening of thin films in narrow confinements.[7] A_{232} will always be a positive value since like substances or solids attract each other over a thin film rendering such a film prone to thinning. Thus, the meniscus curvature is expected to further deform in narrow pore spaces with increasing positives value of A_{232}, the force across the gas enclosed by the meniscus. Figure 7 illustrates the effect of non-retarded and retarded van der Waals surface forces up to the midpoint of a meniscus in apertures of heights $D = 2$ nm and $D = 60$ nm (the depth of the nanochannels). Retardation effects occur when confined molecules are relatively far enough apart that their dipole moments become out of phase faster than the electric field interactions between the molecules, which are limited by the finite speed of light,[46] and are explained in greater detail in Section 3 of the *Supplementary Information*. For effect, the curves in Figure 7 are each compared to the corresponding case where forces from the thinning of the interior gas and opposite side of the meniscus are ignored (blue dotted lines). Values and determination of Hamaker constants for the retarded regime are described in Section 5 of the *Supplementary Information*.

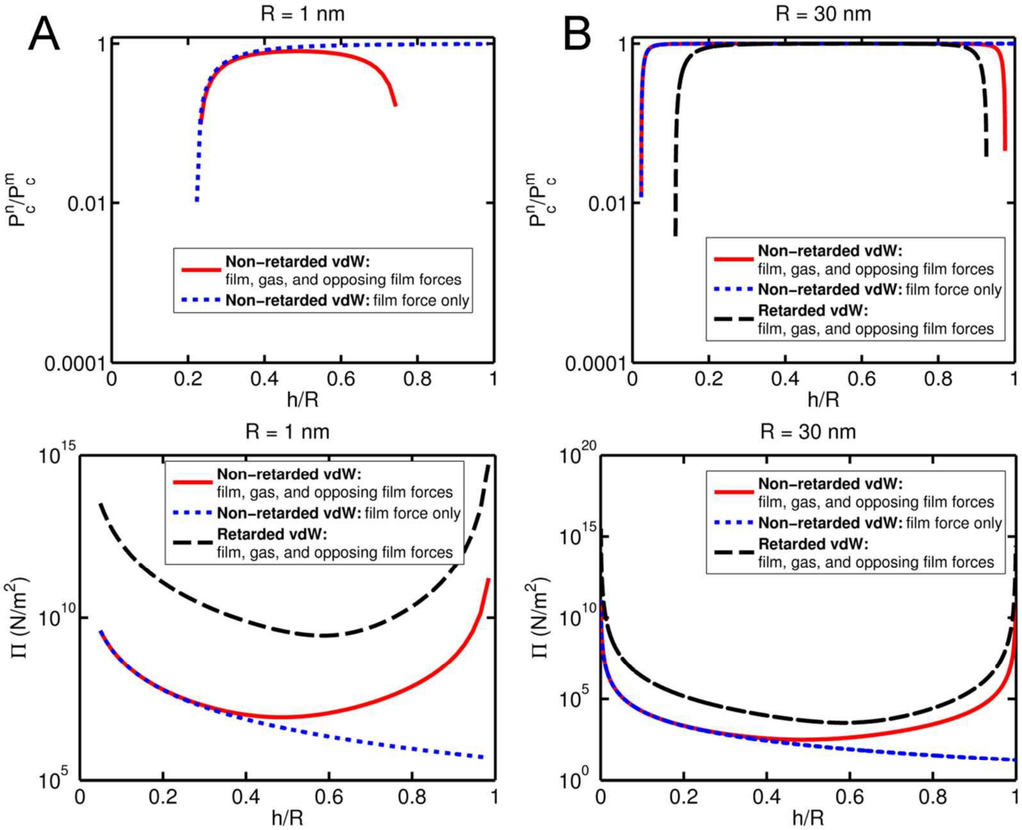

Figure 7. Plots of retarded and non-retarded van der Waals (vdW) forces as a function of meniscus height normalized over 2D channel radius (h/R) for channels of (A) $D = 2$ nm and (B) $D = 60$ nm. Plots of the ratio of the local (non-average) capillary pressure considering these surfaces forces to the macroscopic capillary pressure are

also shown in an analogous manner. Retarded forces are unlikely in nanochannels less than 10 nm in diameter and hence are not plotted for the capillary pressure ratio in the 2 nm diameter channel; the hypothetical values of the retarded force along a 2 nm diameter channel are plotted in the lower panel.

Substitution of Eq.'s 12 and 13 into the relationships in Eq.'s 14 and 16 results in the following ordinary differential equations (ODE) for, respectively, a meniscus where part of the curvature is constant/bulk and a meniscus where no part of the curvature is constant:

$$\gamma \frac{d^2h}{dx^2} = \frac{\gamma \cos\theta_0}{D} + \frac{1}{6\pi}\left(\frac{-A_{123}}{h^3} + \frac{2A_{232}}{(D-2h)^3} - \frac{A_{123}}{(D-h)^3} \right), \ (17)$$

and

$$\gamma \frac{d^2h}{dx^2} = \frac{A_{123}}{6\pi (h_{pre})^3} + \frac{1}{6\pi}\left(\frac{-A_{123}}{h^3} + \frac{2A_{232}}{(D-2h)^3} - \frac{A_{123}}{(D-h)^3} \right). \ (18)$$

The above ODEs can be solved numerically to ascertain *h(x)*, the profile of a nanoscale meniscus curvature as a function of fluid properties and A_H values, nanochannel cross-sectional aperture, and, in some cases, precursor film thickness. However, it is more practical to obtain the average capillary pressure in a nanoscale aperture, $\overline{P}_c^n$, due to the influence surface forces. In addition, the curvature approximation in Eq. 12 is only valid when *dh/dx* is small; that is, the meniscus/film thickness varies slowly. This condition is not the case as *h* approaches $h = 0$ and $h = D/2$, limits which result in an approach toward infinite values of Π_m.

We first approximate the average value of surface forces, $\overline{\Pi}_m$, by integrating Eq. 13 with respect to *h* from precursor film of height h_{pre} (at $x = 0$) to channel radius, *R,* minus half of the minimum width of the minimum stable gas film, d_g, and dividing by this interval. Again, $h = 0$ and $h = D/2$ cannot be used as integrands because they result in infinite values of Π_m. h_{pre} and d_g represent the maximum lengths where surface forces dominate over surface tension and are determined by setting the definition of Π in Eq. 9 equal to the macroscopic capillary pressure value and solving for *d* using, respectively, A_{123} and A_{232}.

Because the shape of the meniscus, *h*(*x*), is unknown, we set *h* to increase linearly between the integrands, thus finding the average of all meniscus/film heights possible in the aperture. Consequently, $\overline{\Pi}_m$ is an estimate. Hence, an estimate of $\overline{P}_c^n$ for a symmetric 2D meniscus with regions of constant and non-constant curvature in the presence of an adsorbed or precursor film of height h_{pre} and within a planar channel or pore space of height *D* is given by

$$\overline{P}_c^n \approx P_c^m - \frac{\int_{h_{pre}}^{R-d_g/2} \Pi_m(h,D)\,dh}{R - \frac{d_g}{2} - h_{pre}} = P_c^m - \frac{\frac{1}{6\pi}\left[\frac{A_{123}}{2}\left(\frac{1}{h^2} - \frac{1}{(D-h)^2} \right) + \frac{A_{232}}{2(D-2h)^2} \right]\Bigg|_{h_{pre}}^{R-d_g/2}}{R - \frac{d_g}{2} - h_{pre}} \ . \ (19)$$

An analogous calculation can be performed for extremely small nanochannels (< ~5 nm in diameter) by replacing P_c^m with Π_f in Eq. 19. There is no surface tension in the expression resulting from that equation because long-range intermolecular force components dominate over capillary pressure.

The previous expressions assumed a 2D meniscus in a slit aperture. Unlike Young Laplace's equation, a calculation of the mean curvature of the normal curvatures, κ_1 and κ_2, along the normal planes at a point in the nanoscale meniscus is inadequate for extension of the meniscus analysis to 3D. That method neglects attractive forces at locations other than along the principal cross sections and will underestimate the degree of meniscus deformation. We use the Derjaguin approximation[42] to extend the 2D analysis of $\bar{P}_c^n$ to a 3D approximation of $\bar{P}_c^n$ in a cylindrical conduit. The Derjaguin approximation states that the *local* disjoining pressure of a curved surface with a certain film system is approximated by the disjoining pressure of a flat surface with the same film system.[42] Some works have used this approximation to determine the shape of a 2D meniscus on a grooved (curved) nanostructured surface.[47] [48] A 3D meniscus in a cylindrical conduit of radius R (D/2) can be considered to be a series of local 2D meniscus film systems whose aperture height, S, changes with the radial distance, r, along the cross section of the conduit. S is determined by the length of a geometrical chord and the average of the disjoining pressure in the cylindrical conduit renders $\bar{P}_c^{n,3D}$, the average 3D nanoscale capillary pressure, namely,

$$\bar{P}_c^{n,3D} \approx P_c^m - \frac{1}{R-h_{pre}} \int_0^{R-h_{pre}} \left(\frac{\displaystyle\int_{h_{pre}}^{(S-d_g)/2} \Pi_m(h,S)\,dh}{\dfrac{S-d_g}{2} - h_{pre}} \right) dr , \quad (20)$$

with

$$S = 2\sqrt{R^2 - r^2} \ . \quad (21)$$

The closed form result of Eq. 20 is shown in Section 4 of the *Supplementary Information*. In non-circular cross sections such as rectangles, S should be described such that the integration will occur from the conduit's largest dimension (diagonal length) to the smallest (a corner).

The ratio of $\bar{P}_c^n$ (in the 2D or 3D form) to the macroscopic capillary pressure predicted by Young-Laplace's equation, P_c^m, can conveniently be expressed as an effective contact angle, θ_{eff}, given by

$$\theta_{eff} = \cos^{-1}\left(\frac{\bar{P}_c^n}{P_c^m} \cos\theta_0 \right), \quad (22)$$

where θ_0 is the macroscopic contact and is equal to zero for perfectly wetting fluids. The effective contact angle convention is useful for practical implementation of nanoscale menisci descriptions because it allows all of the surface force formulations to be encapsulated in a single term and the structure of Young-Laplace's equation remains applicable; i.e. for a cylindrical pore,

$$\overline{P}_c^n = \frac{2\gamma \cos\theta_{eff}}{R}. \quad (23)$$

Figure 8 displays θ_{eff} for the experimental fluids along the range of applicable nanochannel hydraulic diameters. The plot reveals a steep increase in θ_{eff} with a decrease in pore or channel diameter below ~ 10 nm and a difference in θ_{eff} between different fluids for a particular conduit size. The order of these effective contact angles increase from methanol to the hydrocarbons, indicating that the preceding theory correlates with the relative imbibition successes observed in the nanochannel arrays. An exception to this trend is the curve for water; recall from Table 1 that $\theta_0 = 28^\circ$ for water on silica and water is the only one of the tested liquids with a notable macroscopic contact angle. DI water may still have a trace amount of ions present and the extent of the resultant electrical double layer is inversely proportional to ionic concentration. Thus, the curvature of a water meniscus may be subject to electrical double layer and hydration forces, which were not accounted for in this analysis. Also note that the silanol groups at the channel walls may lead to deprotonation or proton uptake effects during the imbibition of aqueous solutions.[49] Effective contact angles for $D = 60$ nm, the depth of all of the nanochannels, are in the arena of ~25-30°. While considerable, these values are nowhere near high enough for the flow to come to a complete stop in the nanochannels. However, the nanochannels are not atomically flat and pinning/contact angle hysteresis effects may be intensified with such deformed menisci. The imbibition data also suggest that the spread of the different values of θ_{eff} between fluids should be more pronounced than Figure 8 indicates. The consideration of elastocapillary deformation in conjunction with meniscus deformation strengthens the explanation of the anomalous imbibition results.

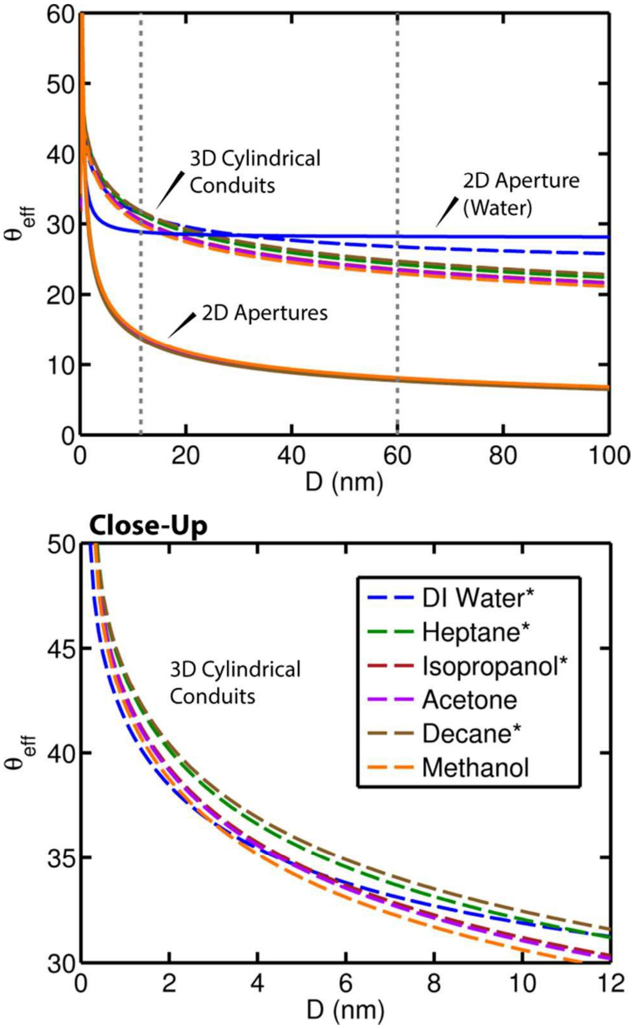

Figure 8. _Solid curves_: effective contact angles for the experimental fluids along the range of applicable nanochannel hydraulic diameters using the result of Eq. 19 (2D case). _Dashed curves_: effective contact angles using the result of Eq. 20 (3D case). θ_{eff} gradually approaches bulk contact angle θ_0 (mainly zero) as hydraulic diameter increases and rises steeply as hydraulic diameter decreases below 10 nm. For example, at D_H = 1 µm, θ_{eff} (3D case) = 14° and θ_{eff} (2D case) = 3° for isopropanol; cos(14°) = 0.970 and cos(3°) = 0.997. Recall that θ_{eff} is not representing an actual contact angle, but a correction due to surface force influences. The lower plot is a close up of the region to the left of the leftmost dotted gray line in the upper plot. The rightmost dotted gray line indicates the etched depth of the nanochannels.

Model for solid deformation

For a wetting fluid, negative liquid pressures behind an imbibing meniscus result in compressive stresses in the wetted areas of a pore space. The resultant stress jump between the wet and dry regions of the pore space lead to decreases in effective pore diameter through shrinkage, buckling, and sometimes channel collapse. Note that the opposite phenomena, expansion, occurs for non-wetting liquids. Per classic mechanical definitions, solid deformations can occur in both the radial (cross-sectional) and axial/longitudinal (along the capillary) directions depending on the elastic properties of the media, the length of the channel or pore, and the thickness of its walls or distance between local pore spaces; however, radial deformations are often negligible. Thin-walled carbon nanotubes are highly susceptible to elastocapillary deformation,[50] and harder materials such as silica also exhibit such fluid-induced deformation.[51]

Liquid pressures are constant within a static trapped liquid plug and the maximum deformation occurs in the center of the plug. During imbibition, liquid pressure drops linearly along the imbibed length of channel or z-direction (see Figure 6.B), and the longitudinal stress vector on the capillary walls, σ_z, scales with the pressure of the imbibing liquid. Hooke's law relates total stress for a given geometry and strain ($\delta l/l$): $\delta l/l = \delta u_z/\delta z = (\sigma_z - \nu(\sigma_x + \sigma_y))/E$, where $u_z(z)$ denotes the local longitudinal deformation for the length imbibed z.[52] The nature of δl is compressive for wetting fluids and the maximum compressive deformation or wall shrinkage is expected to occur in the vicinity of the meniscus front. Shrinkage in the axial direction along a channel will lead to deformations or buckling in the radial direction. Eventually, at length l_c channel convergence or collapse may occur. Bico et al. (2004) and Kim and Mahadevan (2006) provide equations for the determination of l_c during imbibition between parallel sheets;[13] [14] however, the nano-confinements in this work are akin to voids in a solid, not thin-walled tubes or sheets. Love (1929) derived the height deformation in the center of a rectangular area within a semi-infinite solid as a function of pressure.[53]

The aforementioned elastocapillary equations take into account *bulk* mechanical effects, assuming that the surface-induced pressure in the solid is the same as the pressure in the liquid. This assumption is acceptable for macro- and microscopic conduits but is technically incorrect.[54] [55] Following the theory of interfacial zones introduced by Gibbs over a century ago,[54] Figure 6.D depicts how the molecules at a liquid-solid interface are most likely found in a strained and stretched state compared to those of the bulk/interior solid; albeit the effect of stretch is usually on the order of picometers and negligible.[56] Recall that metastable liquids are in tension and pull on the walls of their containers. Thus, surface stresses at the solid interface must be considered at the nanoscale, just as long-range intermolecular forces were considered in tandem with bulk surface tension forces in the previous section. Weissmüller and Cahn (1996) and Weissmüller (2010) provide a generalized capillary equation for the average pressure in the solid bulk, P_s, as a function of enclosed fluid pressure, P_f, the specific surface area (interfacial area, A_s, per solid volume, V_s) of the pore space, ξ, elastic strain, ε, and average (scalar) surface stress at the interface, f_I (units of N/m):[57] [56]

$$P_s = P_f + \frac{2}{3}\zeta f_I \ , \quad (24)$$

$$f_I = \gamma + \frac{d\gamma}{d\varepsilon} \ , \quad (25)$$

and

$$\zeta = \frac{A_{surface}}{V_s} \ . \quad (26)$$

For a cylindrical void (an approximation of the geometry of the tested nanochannels), $\xi = 2/(r(1\text{-}\phi))$, where ϕ is void porosity and very small for the nanochip configuration; i.e. $1\text{-}\phi \approx 1$. Local longitudinal deformation in arrays of channels as a function of distance along the axial direction of an imbibition front, $z(t)$, is then described by:[56]

$$u_z = \frac{1}{2}\left(P_f + \frac{2}{3}\zeta \bar{f}_I\right)\frac{1}{K}\frac{1-\nu}{2\nu-1}z(t)\,, \quad (27)$$

and

$$K = \frac{E}{3(1-2\nu)}\,, \quad (28)$$

where E is Young's modulus, ν is Poisson's ratio, and x is position along the length of the channel. We posit that the local solid shrinkage in the longitudinal directional will manifest itself as a decrease in channel cross sectional area. Thus, u_z is an estimate of decrease in diameter, and at $z = l_c$, u_z is approximately equal to the smallest critical dimension of the channel; this dimension is 60 nm for the majority of the studied nanochannels. Thus, the model does not explicitly predict when the imbibition front should stop, but predicts when a channel will collapse in its smallest direction, significantly increasing flow resistance. At this point, the cross-sectional area may become separated into limited spaces (see Figure 6.C). Equations for independent displacement in the radial direction are available as well,[56 58] but their effects are small compared to the longitudinal case.

Eq. 25 is the Shuttleworth equation.[59] Unfortunately, it is challenging to determine f_I without stress-strain data. For reference, values of f_I for metals are usually around 1 N/m.[56] Figure 9 displays curves of l_c/L (plotted in black) for different values of f_I against the imbibition termination lengths; recall that L is the length of the nanochannels.

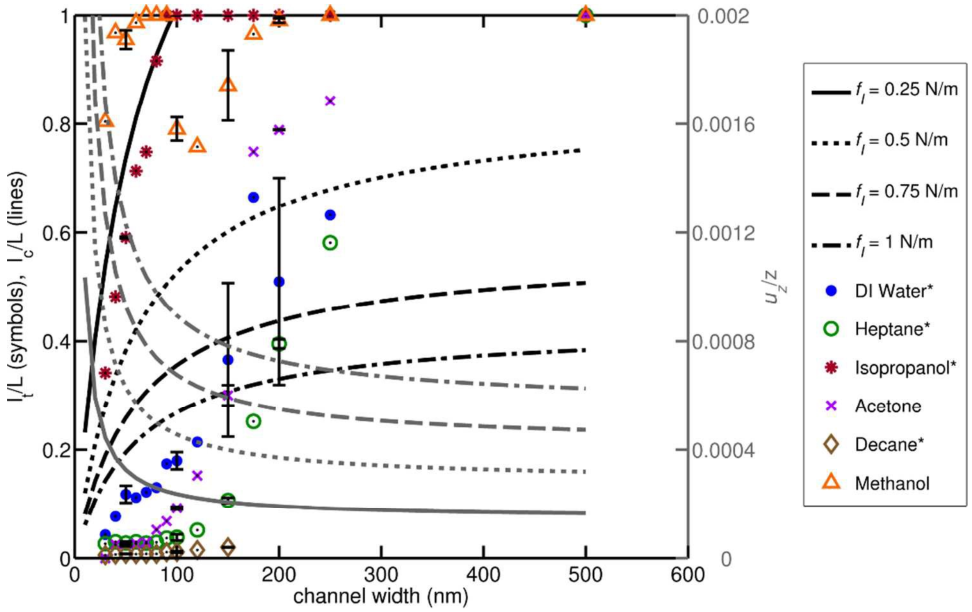

Figure 9. Black curves go with the left y-axis while gray curves go with the right y-axis. Curve patterns correspond to surface stress values, f_l. When l_t/L data points fall below one of the black curves, the imbibition front is stopped by the combined effect of an increase in hydraulic resistance and decrease in capillary pressure. When l_t/L data points fall above one of these curves, the capillary pressure is lower than predicted, but still strong enough to overcome the corresponding hydraulic resistance. Gray curves describe the amount of deformation experienced by the pore cross-section per the length imbibed; deformation rises dramatically in channels less than 100 nm in critical dimension. Channel deformation is expressed in terms of u_z/z (the right y-axis), where z is length imbibed, because u_z scales linearly with z (see Eq. 27) and has a slope dependent on material, channel, and fluid properties: f_l , ξ, P_f, K, and ν. Thus, for any channel width, w, and z, $(u_z/z)*z$ renders u_z; u_z values are on the order of nanometers when z is on the order of microns. Relevant elastic parameters for silica: E = 73 GPa and ν = 0.2. Fluid parameters used for constructing curves: θ_{eff} = 0 and γ = 0.02 N/m.

In axially convergent channels, liquid is expected to imbibe *faster* and *beyond* the length and rate predicted by the Washburn equation in the limit of channel collapse and increased viscous dissipation.[60 61] The termination length data presented herein suggest otherwise; that is, they suggest that the smaller of the observed nanochannels are deformed such that their effective diameter is small enough at the region of the front to reach a threshold of significant meniscus deformation (in Figure 8, observe the nature of the curves below ~ D = 10 nm). This compounded deformation of channel and meniscus contributes to the eventual stopping of an imbibing liquid front, possibly before its respective l_c curves in Figure 9. Increased μ_{eff}, discussed subsequently, contributes to the premature stoppage as well.

Recall that in our previous publication[16] the imbibition of isopropanol in arrays of silica nanochannels equivalent to those in this work did not follow a diffusive trend in the array's larger nanochannels. Instead, the imbibition approached a linear trend, even though the velocity was slower than predicted.[16] Theoretically, a converging channel leads to increases in capillary pressure with length imbibed and an exponent of the imbibition time greater than 0.5. This relationship only manifests itself in the largest nanochannels in the array, where channel deformations, viscous losses, and menisci deformations (per the analysis of the preceding section) are predicted to be least. These data points often fall above l_c curves in Figure 9.

The interpretation of the Shuttleworth equation is highly debated and the topic of interfacial surface stresses is generally under-researched. Materials are inclined to have decreased Young's moduli, or "soften", at interfaces because atomic coordination is less at surfaces.[62] The data evidence the significance of surface stress and resulting strain and "interface softening" at the nanoscale; i.e. predicted l_c values were only comparable to l_t when Eq. 27 was used. When it is assumed that only capillary pressure contributes to the surface induced pressure in the bulk, or $P_s = P_f$, the black curves of l_c/L in Figure 9, plotted as a function of θ_{eff}, shift upward to the range of l_c/L = 1-10 and do not exhibit much separation.

In some situations (e.g. geological porous media), additional deformations can be caused by external forces,[63] but only stresses due to capillary and interfacial effects need to be considered in this work. It is unclear whether the described changes to the nanochannels are plastic (permanent) or elastic (temporary). Additionally, it is possible that some reports of higher effective viscosity in nano-confinements may be misinterpretations of solid interface deformation.

Models for effective diameter and liquid viscosity

Overall, channel deformations lead to a decrease in effective diameter and, hence a decrease in hydraulic conductivity or permeability (for porous media). When the cross sectional area of a nanoscale channel or pore is severely decreased, the aforementioned viscosity effects described by Eq.'s 4-6 arise. Effective channel diameter, D_{eff}, due to elastocapillary and surface deformation effects, and effective viscosity, μ_{eff}, the evaluation of Eq. 5 at D_{eff}, are defined as:

$$D_{eff} = 2\left(R - \Delta r_{elastic} - \Delta r_{film} - \Delta r_{q.c.} - \Delta r_{adsorbed}\right), \quad (29)$$

and

$$\frac{\mu_{eff}}{\mu_{bulk}} = \left.\frac{\mu_{nano}}{\mu_{bulk}}\right|_{D_{eff}}, \quad (30)$$

where R is the radius or hydraulic radius of a dry channel or pore and $\Delta r_{elastic}$ is equal to u_z and due to both radial (when applicable) and axial deformations (a function of length imbibed); Δr_{film} encompasses adsorbed, pre-wetting, and solute films; $\Delta r_{q.c.}$ describes the quasi-crystalline layer(s) of fluid molecularly bound to the solid; and $\Delta r_{adsorbed}$ is the thickness of residue left by the adsorption of dissolved substances at a the three-phase contact line[39]. Both D_{eff} and μ_{eff} are non-constant. Figure 10 displays how viscosity diverges from its bulk value for the tested fluids near solid interfaces per the model in Eq.'s 4-6. Upon deformation and opposite wall contact channel cross sections drastically narrow and regions of such enhanced viscosity are possible. Liquid-specific properties are incorporated into the model as follows:

$$\Delta G_I = \frac{A_{12}}{6\pi D^3 \rho_s} = \frac{\sqrt{A_{11}}\sqrt{A_{22}} M_w}{6\pi D^3 \tilde{N} \rho}, \quad (31)$$

where A_{12} is the Hamaker constant for materials/fluids 1 and 2 acting across a vacuum, ρ is fluid density (units of kg/m^3), and M_w is molecular weight. $A_{22} \approx A_{232}$ and for silica $A_{11} = 6.53 \times 10^{-20}$. A relationship between Hamaker constants and imbibition success by way of increased viscosity at surfaces is evident.

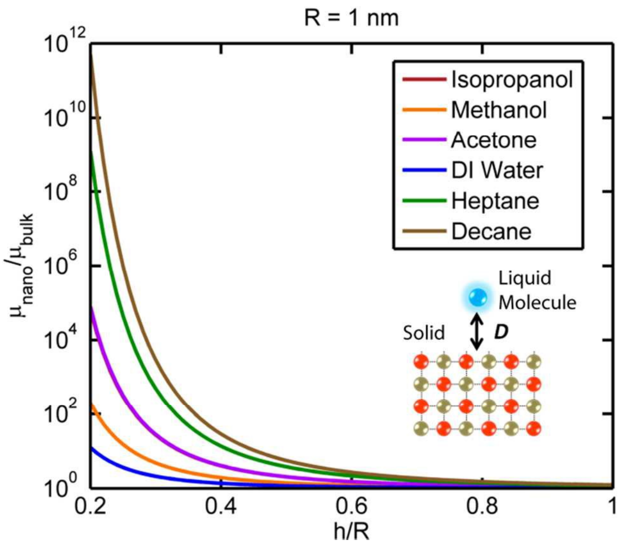

Figure 10. Model for divergence of viscosity from its bulk value near a solid interface (at *h* =0) for the tested fluids. Curves for isopropanol and methanol overlap. The hydrocarbons, especially decane, exhibit the greatest divergence near surfaces; decane also imbibed the least. The diagram refers to the model which the enhanced viscosity is derived from: additional energy on fluid molecules near interfaces due to interactions with solid molecules.

Dimensionless Number Index

We propose a dimensionless number designated by the Greek letter Λ for the ratio of average surface forces acting over a meniscus (van der Waals, electrostatic, etc.) to bulk capillary forces in a representative conduit or pore size:

$$\Lambda = \frac{\bar{\Pi}_m}{P_c^m} \quad . (32)$$

When $\Lambda \ll 1$ the influence of surface forces is insignificant and the classic Young-Laplace equation is sufficient. When $\Lambda \approx 1$, a portion of the meniscus is still dominated by bulk values (constant curvature), but surface forces create non-negligible deformations in regions closer to solid interfaces. The classic Young-Laplace equation is insufficient for proper description of these menisci. Eq. 14 is applicable in this range and an effective contact angle can be found such as is presented in this work. Finally, in the case where $\Lambda \gg 1$, surface forces are very significant and virtually no part of the meniscus exhibits constant curvature; i.e. the classic Young-Laplace equation fails. Eq. 16 is applicable for these channels and an average capillary pressure can be obtained with Eq. 20 where P_c^m is replaced by Π_f.

A considerable change in effective channel or pore diameter can occur due to elastocapillary deformation and adsorbed films. Likewise, an effective liquid viscosity, primarily a product of the decrease in channel size and potentially non-constant, must be considered instead of a bulk value when the deformed or initial diameter of nano-confinements approach the length scale of solvation forces. A simple dimensionless index designated by the Greek letter Γ for assessment of the need to consider D_{eff} and μ_{eff} is the ratio of the characteristic collapse length to the length of the media or the imbibition length of interest, namely,

$$\Gamma = \frac{l_c}{L}. \quad (33)$$

When $\Gamma \leq 1$, effective liquid viscosity should be considered. Calculations of l_c will vary between media; however, the equations for deformation along the axial direction have been found to be the same among fiber networks and solids with either spherical or cylindrical pores.[56] Recall that l_c is a function of the (average) pore or conduit size, specific surface area, fluid pressure, surface stress, and the bulk elastic properties of a media. Eq. 27 can also be used for dimensionless scaling of pore deformation effects when both sides of the equation are divided by $z(t)$.

Γ should be assessed first and if $\Gamma \leq 1$, then Λ be assessed at an effective pore diameter. A visual diagram of the dimensionless numbers and deformation regimes is included in Section 6 of the *Supplementary Information*.

CONCLUSIONS AND IMPLICATIONS

An investigation into the mechanisms behind anomalous imbibition of various liquids in lyophilic 2D nanochannels revealed the need to consider the deformation of fluids and solids at interfaces. The major conclusions and contributions of the work are as follows:

- Macroscopic descriptions of imbibition are insufficient in fully nanoscale (2D) confinements because they do not consider menisci deformation due to long-range intermolecular forces and effective pore space deformation due to thin films and elastocapillarity and surface stresses. These effects increase sensitivity to surface area to volume ratio and were most prominent in the smallest nanochannels observed (30 nm × 60 nm).
- Liquids with low A_{232} and high absolute values of A_{123} imbibed the most effectively in the 2D nanochannels. The latter indicates that despite decreasing the effective channel diameter, precursor films may have a positive effect on nanoscale imbibition in such confinements.
- We presented phenomenological models for effective contact angle, effective diameter, and effective viscosity which explain our nanofluidic data and potentially the nanofluidic works of others.
- We demonstrated that the Young-Laplace equation breaks down as a function of several parameters: channel diameter, Hamaker constants, the height of a pre-wetting film, and surface tension. The derivations are based on surface-force theories (the works of Derjaguin, Israelachvili, Langbein, Hamaker, Lifshitz, etc., all referenced herein), which conveniently enable molecular interactions to be described from a continuum perspective.

- The dimensionless ratio Λ, introduced herein, can be used to determine when the Young-Laplace equation is reliable, when a modified version of the Young-Laplace equation is required, or when the Young-Laplace equation is no longer applicable.
- Longitudinal elastocapillary deformations of a confinement are functions of channel or pore size, capillary and liquid pressure, specific surface area, position, and the bulk elastic properties of a media. A dimensionless ratio of the length of pore collapse to the length of interest of the media can be used to determine when elastocapillary effects are prominent and D_{eff} and μ_{eff} necessary.
- The nanochannel data verify the necessity of considering solid surface stress in addition to surface tension, a consideration often ignored at larger scales. The corollary of this consideration is that the elastic properties at solid silica interfaces differ from the bulk elastic properties; i.e. the silica is "softer" in the interfacial region.
- Overall, meniscus deformation and increases in effective viscosity are exacerbated by elastocapillary deformation, while elastocapillary deformation is exacerbated by negatively pressured and metastable liquids. These phenomena converge in the studied nanochannels to stymie imbibition and are likely in other nanoscale media.

Improved descriptions of nanoscale imbibition and menisci is of importance to a variety of biological, geophysical, and technological topics, including transport and liquid loss in nanoporous (unconventional) hydrocarbon-bearing media, soil science, groundwater flow, carbon capture and sequestration; transport in nanoporous organs; cavitation in internal medicine; lab-on-a-chip drug delivery systems; and function-based nanofluidic devices. Tuning of a system's Hamaker constant by fluid solvent and solute selection can potentially enhance or decrease fluid imbibition and drainage effects as needed. Changes in the dimensions of a nanoporous media or conduit can potentially be used to characterize either the intrinsic capillary forces or mechanical properties of the solid. Specifically, elastocapillarity can be externally controlled with methods such as electric fields,[64] and implemented as a diagnostic method for investigating the internal structure of complex nanoporous media. Modeling and further experimental verification based on this work, especially probing the influence of surface asperities, are encouraged.

ACKNOWLEDGEMENTS

We thank the University of Texas at Austin's Institute for Cellular and Molecular Biology for the use of their microscopy equipment. We acknowledge NIL Technology for their assistance in nanofluidic chip fabrication. This research was supported by the American Chemical Society Petroleum Research Fund (Grant #: 52817-ND9) and the University of Texas at Austin's Formation Evaluation Research Consortium, jointly sponsored by Afren, Anadarko, Apache, Aramco, Baker-Hughes, BG, BHP Billiton, BP, Chevron, China Oilfield Services LTD., ConocoPhillips, Det Norske, ENI, ExxonMobil, Halliburton, Hess, Maersk, Mexican Institute for Petroleum, ONGC, OXY, Petrobras, PTT Exploration and Production, Repsol, RWE, Schlumberger, Shell, Southwestern Energy, Statoil, TOTAL, Weatherford, Wintershall and Woodside Petroleum Limited.

REFERENCES

1 M. R. Stukan, P. Ligneul, J. P. Crawshaw and E. S. Boek, *Langmuir*, 2010, **26**, 13342–13352.

2 M. Rauscher and S. Dietrich, *Annu. Rev. Mater. Res.*, 2008, **38**, 143–172.

3 N. V. Churaev, *Rev. Phys. Appliquée*, 1988, **23**, 975–987.

4 P. G. de Gennes, *Rev. Mod. Phys.*, 1985, **57**, 827–863.

5 K. Chaudhury, P. V. Acharya and S. Chakraborty, *Phys. Rev. E*, 2014, **89**, 053002.

6 B. V. Derjaguin, N. V. Churaev and V. M. Muller, in *Surface Forces*, Springer US, 1987, pp. 1–23.

7 B. V. Derjaguin and N. V. Churaev, *J. Colloid Interface Sci.*, 1976, **54**, 157–175.

8 P. Kim, H.-Y. Kim, J. K. Kim, G. Reiter and K. Y. Suh, *Lab. Chip*, 2009, **9**, 3255–3260.

9 J. W. van Honschoten, N. Brunets and N. R. Tas, *Chem. Soc. Rev.*, 2010, **39**, 1096–1114.

10 F. M. Etzler and D. M. Fagundus, *J. Colloid Interface Sci.*, 1987, **115**, 513–519.

11 G. Peschel and K. H. Adlfinger, *J. Colloid Interface Sci.*, 1970, **34**, 505–510.

12 G. H. Pollack, *The Fourth Phase of Water: Beyond Solid, Liquid, and Vapor*, Ebner & Sons, 2013.

13 J. Bico, B. Roman, L. Moulin and A. Boudaoud, *Nature*, 2004, **432**, 690–690.

14 H.-Y. Kim and L. Mahadevan, *J. Fluid Mech.*, 2006, **548**, 141–150.

15 B. Roman and J. Bico, *J. Phys. Condens. Matter*, 2010, **22**, 493101.

16 S. A. Kelly, M. T. Balhoff and C. Torres-Verdin, *Langmuir*, 2015.

17 E. W. Washburn, *Phys. Rev.*, 1921, **17**, 273–283.

18 J. T. Mannion, C. H. Reccius, J. D. Cross and H. G. Craighead, *Biophys. J.*, 2006, **90**, 4538–4545.

19 K. S. Birdi, *Handbook of Surface and Colloid Chemistry, Third Edition*, CRC Press, 2008.

20 Edgar F. Ethington, *Interfacial Contact Angle Measurements of Water, Mercury, and 20 Organic Liquids on Quartz, Calcite, Biotite, and Ca-montmorillonite Substrates*, U.S. Geological Survey, 1990, vol. 90.

21 R. Holyst, A. Bielejewska, J. Szymański, A. Wilk, A. Patkowski, J. Gapiński, A. Żywociński, T. Kalwarczyk, E. Kalwarczyk, M. Tabaka, N. Ziębacz and S. A. Wieczorek, *Phys. Chem. Chem. Phys.*, 2009, **11**, 9025.

22 S. S. Jang, S.-T. Lin, P. K. Maiti, M. Blanco, W. A. Goddard, P. Shuler and Y. Tang, *J. Phys. Chem. B*, 2004, **108**, 12130–12140.

23 E. Vandre, M. S. Carvalho and S. Kumar, *J. Fluid Mech.*, 2012, **707**, 496–520.

24 A. Siebold, M. Nardin, J. Schultz, A. Walliser and M. Oppliger, *Colloids Surf. Physicochem. Eng. Asp.*, 2000, **161**, 81–87.

25 F. F. Ouali, G. McHale, H. Javed, C. Trabi, N. J. Shirtcliffe and M. I. Newton, *Microfluid. Nanofluidics*, 2013, **15**, 309–326.

26 R. Seemann, M. Brinkmann, E. J. Kramer, F. F. Lange and R. Lipowsky, *Proc. Natl. Acad. Sci. U. S. A.*, 2005, **102**, 1848–1852.

27 A. Ponomarenko, D. Quéré and C. Clanet, *J. Fluid Mech.*, 2011, **666**, 146–154.

28 J. Bico and D. Quéré, *Europhys. Lett. EPL*, 2003, **61**, 348–353.

29 L. H. Thamdrup, F. Persson, H. Bruus, A. Kristensen and H. Flyvbjerg, *Appl. Phys. Lett.*, 2007, **91**, 163505.

30 A. R. Imre, H. J. Maris and P. R. Williams, *Liquids Under Negative Pressure: Proceedings of the NATO Advanced Research Workshop of Liquids Under Negative Pressure Budapest, Hungary 23-25 February 2002*, Springer Science & Business Media, 2002.

31 T. D. Wheeler and A. D. Stroock, *Nature*, 2008, **455**, 208–212.

32 S. C. Maroo and J. N. Chung, *Nanoscale Res. Lett.*, 2011, **6**, 1–7.

33 P. G. Debenedetti, *Nat. Phys.*, 2013, **9**, 7–8.

34 B. Bhushan, *Scanning Probe Microscopy in Nanoscience and Nanotechnology 2*, Springer Science & Business Media, 2010.

35 C. E. Brennen, *Cavitation and Bubble Dynamics*, Cambridge University Press, 2013.

36 R. Zhang, Y. Ikoma and T. Motooka, *Nanotechnology*, 2010, **21**, 105706.

37 C. Duan, R. Karnik, M.-C. Lu and A. Majumdar, *Proc. Natl. Acad. Sci. U. S. A.*, 2012, **109**, 3688–3693.

38 R. B. Bird, W. E. Stewart and E. N. Lightfoot, *Transport Phenomena*, John Wiley & Sons, 2007.

39 H.-J. Butt, K. Graf and M. Kappl, *Physics and Chemistry of Interfaces*, John Wiley & Sons, 2006.

40 C. Liu and Z. Li, *AIP Adv.*, 2011, **1**, 032108.

41 J. C. Berg, *An Introduction to Interfaces & Colloids: The Bridge to Nanoscience*, World Scientific, 2010.

42 J. Weissmüller and D. Kramer, *Langmuir*, 2005, **21**, 4592–4603.

43 D. Langbein, *J. Adhes.*, 1972, **3**, 213–235.

44 J. N. Israelachvili, *Intermolecular and Surface Forces: Revised Third Edition*, Academic Press, 2011.

45 J. N. Israelachvili and D. Tabor, *Proc. R. Soc. Lond. Math. Phys. Eng. Sci.*, 1972, **331**, 19–38.

46 B. V. Derjaguin, N. V. Churaev and V. M. Muller, in *Surface Forces*, Springer US, 1987, pp. 25–52.

47 H. Hu, C. R. Weinberger and Y. Sun, *Nano Lett.*, 2014, **14**, 7131–7137.

48 M. O. Robbins, D. Andelman and J. F. Joanny, *Phys. Rev. A*, 1991, **43**, 4344–4354.

49 K. G. H. Janssen, H. T. Hoang, J. Floris, J. de Vries, N. R. Tas, J. C. T. Eijkel and T. Hankemeier, *Anal. Chem.*, 2008, **80**, 8095–8101.

50 M. P. Rossi, Y. Gogotsi and K. G. Kornev, *Langmuir*, 2009, **25**, 2804–2810.

51 G. Günther, J. Prass, O. Paris and M. Schoen, *Phys. Rev. Lett.*, 2008, **101**, 086104.

52 Daria Monaenkova, Clemson University, 2012.

53 A. E. H. Love, *Philos. Trans. R. Soc. Lond. Ser. Contain. Pap. Math. Phys. Character*, 1929, **228**, 377–420.

54 H. L. Duan, J. Wang, Z. P. Huang and B. L. Karihaloo, *Proc. R. Soc. Lond. Math. Phys. Eng. Sci.*, 2005, **461**, 3335–3353.

55 Y. Z. Povstenko, *J. Mech. Phys. Solids*, 1993, **41**, 1499–1514.

56 J. Weissmüller, H.-L. Duan and D. Farkas, *Acta Mater.*, 2010, **58**, 1–13.

57 J. Weissmüller and J. W. Cahn, *Acta Mater.*, 1997, **45**, 1899–1906.

58 T. B. Hoberg, E. Verneuil and A. E. Hosoi, *Phys. Fluids 1994-Present*, 2014, **26**, 122103.

59 R. Shuttleworth, *Proc. Phys. Soc. Sect. A*, 1950, **63**, 444.

60 J. M. Aristoff, C. Duprat and H. A. Stone, *Int. J. Non-Linear Mech.*, 2011, **46**, 648–656.

61 T. Cambau, J. Bico and E. Reyssat, *EPL Europhys. Lett.*, 2011, **96**, 24001.

62 L. G. Zhou and H. Huang, *Appl. Phys. Lett.*, 2004, **84**, 1940–1942.

63 C. G. Eggers, M. Berli, M. L. Accorsi and D. Or, *J. Geophys. Res. Solid Earth*, 2006, **111**, B10204.

64 M. Piñeirua, J. Bico and B. Roman, *Soft Matter*, 2010, **6**, 4491–4496.